Cell Reports
Physical Science

CellPress
OPEN ACCESS

Article

Photochemical production of hydrogen peroxide by digging pro-superoxide radical carbon vacancies in porous carbon nitride

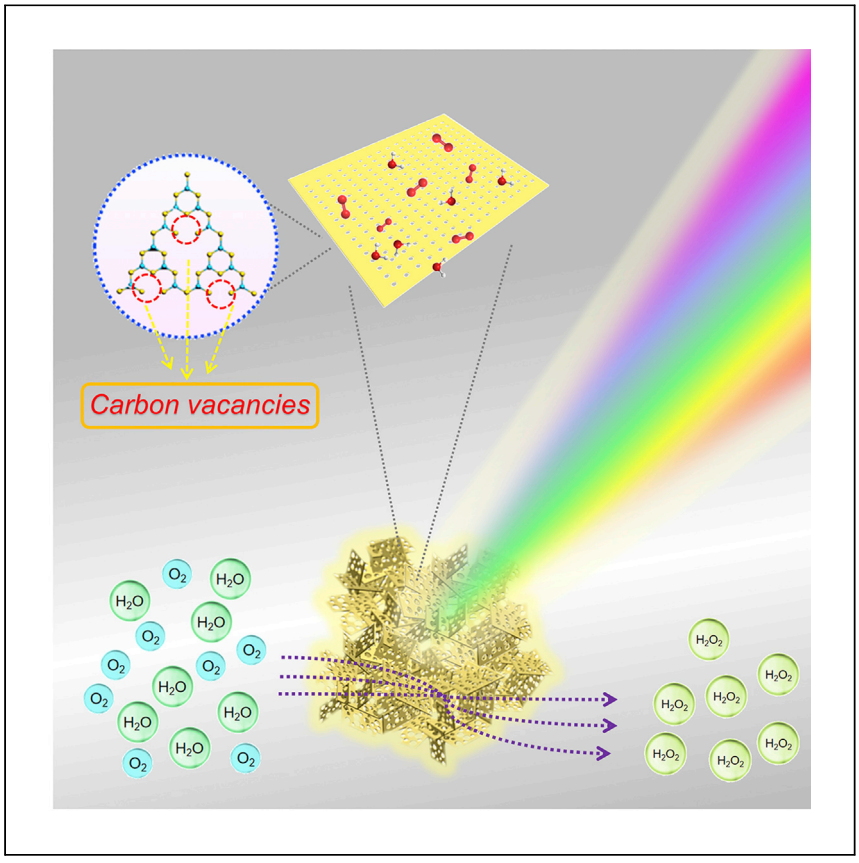

Ding et al. report an innovative hydrolysis-freeze-drying-thermal treatment method for fabricating a 3D hierarchical porous carbon nitride with carbon vacancies. Owing to the synergistic effects between the carbon vacancies and the unique 3D hierarchical porous structure, the highly efficient photocatalytic H_2O_2 production is achieved.

Yang Ding, Soumyajit Maitra, Daniel Arenas Esteban, ..., Yu Li, Alexandru Vlad, Bao-Lian Su

yu.li@whut.edu.cn (Y.L.)
bao-lian.su@unamur.be (B.-L.S.)

Highlights

Innovative hydrolysis-freeze-drying-thermal treatment (HFDT) method

3D hierarchical porous carbon nitride (g-C_3N_4) with carbon vacancies

H_2O_2 evolution rate of 6287.5 μM g^{-1} h^{-1} with an outstanding long cycling stability

Modulating electronic structure and promoting H_2O_2 evolution through carbon vacancies

Ding et al., Cell Reports Physical Science 3, 100874
May 18, 2022
https://doi.org/10.1016/j.xcrp.2022.100874

Cell Reports
Physical Science

CellPress
OPEN ACCESS

Article

Photochemical production of hydrogen peroxide by digging pro-superoxide radical carbon vacancies in porous carbon nitride

Yang Ding,[1,2] Soumyajit Maitra,[3] Daniel Arenas Esteban,[4] Sara Bals,[4] Henk Vrielinck,[5] Tarek Barakat,[1,2] Subhasis Roy,[3] Gustaaf Van Tendeloo,[4] Jing Liu,[6] Yu Li,[6,*] Alexandru Vlad,[7] and Bao-Lian Su[1,2,8,9,*]

SUMMARY

Artificial photosynthesis of H_2O_2, an environmentally friendly oxidant and a clean fuel, holds great promise. However, improving its efficiency and stability for industrial implementation remains highly challenging. Here, we report the visible-light H_2O_2 artificial photosynthesis by digging pro-superoxide radical carbon vacancies in three-dimensional hierarchical porous g-C_3N_4 through a simple hydrolysis-freeze-drying-thermal treatment. A significant electronic structure change is revealed upon the implantation of carbon vacancies, broadening visible-light absorption and facilitating the photogenerated charge separation. The strong electron affinity of the carbon vacancies promotes superoxide radical ($^{\cdot}O_2^-$) formation, significantly boosting the H_2O_2 photocatalytic production. The developed photocatalyst shows an H_2O_2 evolution rate of 6287.5 $\mu M\ g^{-1}\ h^{-1}$ under visible-light irradiation with a long cycling stability being the best-performing photocatalyst among all reported g-C_3N_4-based systems. Our work provides fundamental insight into highly active and stable photocatalysts with great potential for safe industrial H_2O_2 production.

INTRODUCTION

As an important chemical reagent, H_2O_2 is widely used for chemical synthesis and environmental remediation. Moreover, H_2O_2 is also considered a potential clean energy alternative for substituting conventional hydrogen energy due to its comparable energy density.[1–6] Various strategies, including electrochemical synthesis, alcohol oxidation, and anthraquinone oxidation (AO) processes, have been developed so far to prepare H_2O_2.[7–10] The most used commercial route is the AO process.[9] However, the high cost, tedious operation, and virulent by-products emission of the AO process lead to important efforts in finding efficient, safe, and environmentally friendly alternatives for large-scale production of H_2O_2. The electrocatalytic oxygen reduction reaction (ORR) is recognized as a strong candidate; however, the vast energy consumption and high risk of explosion due to the mixture of H_2 and O_2 hinder its industrial implementation.[10]

Artificial photosynthesis has been regarded as one of the most promising technologies to overcome the energy and environmental challenges.[11–15] It has been reported that upon solar-light irradiation, the photocatalysts can generate photoinduced electrons able to reduce the molecular oxygen, leading to the formation of hydrogen peroxide.[9] Compared with the electrochemical synthesis and the AO process, the artificial photosynthesis of H_2O_2 exhibits multiple advantages, such as low

[1]Laboratory of Inorganic Materials Chemistry (CMI), University of Namur, Rue de Bruxelles 61, 5000 Namur, Belgium

[2]Namur Institute of Structured Matter (NISM), University of Namur, Rue de Bruxelles 61, 5000 Namur, Belgium

[3]Department of Chemical Engineering, University of Calcutta, 92 APC Road, West Bengal, Kolkata 700009, India

[4]Electron Microscopy for Materials Science (EMAT), University of Antwerp, 2020 Antwerp, Belgium

[5]Department of Solid State Sciences, Ghent University, Krijgslaan 281-S1, 9000 Gent, Belgium

[6]State Key Laboratory of Advanced Technology for Materials Synthesis and Processing, Wuhan University of Technology, 122 Luoshi Road, 430070 Wuhan, Hubei, China

[7]Institute of Condensed Matter and Nanosciences, Université Catholique de Louvain, Place Louis Pasteur 1/L4.01.02, 1348 Louvain-la-Neuve, Belgium

[8]Clare Hall, University of Cambridge, Cambridge CB2 1EW, UK

[9]Lead contact

*Correspondence: yu.li@whut.edu.cn (Y.L.), bao-lian.su@unamur.be (B.-L.S.)

https://doi.org/10.1016/j.xcrp.2022.100874

energy consumption and a considerably reduced environmental impact.[16–18] Yamashita's group reported hydrophobic metal-organic frameworks (MOFs) to promote the H_2O_2 production in a two-phase benzyl alcohol/water system,[14] whereas Xu et al. proposed a new two-electron water oxidation pathway using acethylene and diacethylene functional covalent triazine frameworks.[1] Graphitic carbon nitride (g-C_3N_4) has attracted increasing attention in solar energy conversion and shows very promising performances for photocatalytic H_2O_2 production.[19–28] Choi's group reported a heteroatom doping of polymeric C_3N_4 for H_2O_2 production enhancement,[7] whereas holey nitrogen-defective g-C_3N_4 with abundant exposed active sites presented a higher H_2O_2 production activity compared with bulk g-C_3N_4.[24] Oxygen-enriched g-C_3N_4,[15] g-C_3N_4/aromatic diimide/graphene nanohybrids,[3] and leaf-vein-like g-C_3N_4[27] have been also found to improve the efficiency of the H_2O_2 production by promoting the photoinduced charge carrier separation. A significant enhancement in photocatalytic H_2O_2 output using atomic Sb particle loaded g-C_3N_4 was achieved by promoting a two-electron oxygen reduction.[28] Additionally, g-C_3N_4-based photonic crystals have also been shown to accelerate the photocatalytic H_2O_2 production by enhancing visible-light absorption.[16] However, the efficiency of these H_2O_2 photosynthesis processes and stability of the photocatalysts are still far away from industrial requirements, severely impeding their practical applications, and its improvement remains a great scientific and practical challenge.[9]

Here, we report the implantation of carbon vacancies in 3D hierarchical porous C_3N_4 scaffolds through an innovative hydrolysis-freeze-drying-thermal treatment (HFDT) method. The introduction of well-modulated carbon vacancies in the 3D hierarchical porous C_3N_4 scaffold leads to an unprecedentedly high H_2O_2 evolution rate of 6287.5 μM g^{-1} h^{-1} under visible-light irradiation. This is the highest value attained so far when compared with literature reports, and 4.2 and 1.6 times higher than that of the bulk g-C_3N_4 and g-C_3N_4 nanosheets, respectively. The cycling study of our photocatalysts with a very long cycle of 10 h shows an outstanding stability up to 100 h, the best stability and the longest cycle duration compared with the state-of-the-art reports. Fukui function (FF) and electrostatic potential plots reveal the essential role of carbon vacancies as reaction active sites, with a strong electron affinity and $^{\bullet}O_2^-$ radicals generating ability, all being favorable for the enhanced photocatalytic H_2O_2 generation. The significantly improved photosynthetic H_2O_2 production activity is thus attributed to the generation of a mid-gap electronic level upon the introduction of carbon vacancies, which extends the absorption in the visible-light range, facilitates the photoinduced charge separation,[25–27] and promotes the $^{\bullet}O_2^-$ radicals formation. Moreover, the highly exposed surface of the 3D hierarchical porous structure offers abundant reactive sites and developed porous channels for the fast mass transfer of the reactants and products.[29–35] This innovative freeze-drying process inducing carbon vacancies can be extended for the preparation of highly active carbon-defective materials for other photocatalytic applications. Our carbon-deficient hierarchical porous g-C_3N_4 consolidates its potential as a highly efficient photocatalyst for the large-scale and safe industrial production of H_2O_2.

RESULTS AND DISCUSSION

Morphology and structure characterizations

Figures 1A and 1B depict the fabrication process of the carbon-deficient 3D hierarchical porous C_3N_4 scaffold through an innovative HFDT of melamine. Compared with the traditional preparation route (Figure 1C), the innovative HFDT method can simultaneously induce carbon vacancies and create a 3D hierarchical porous

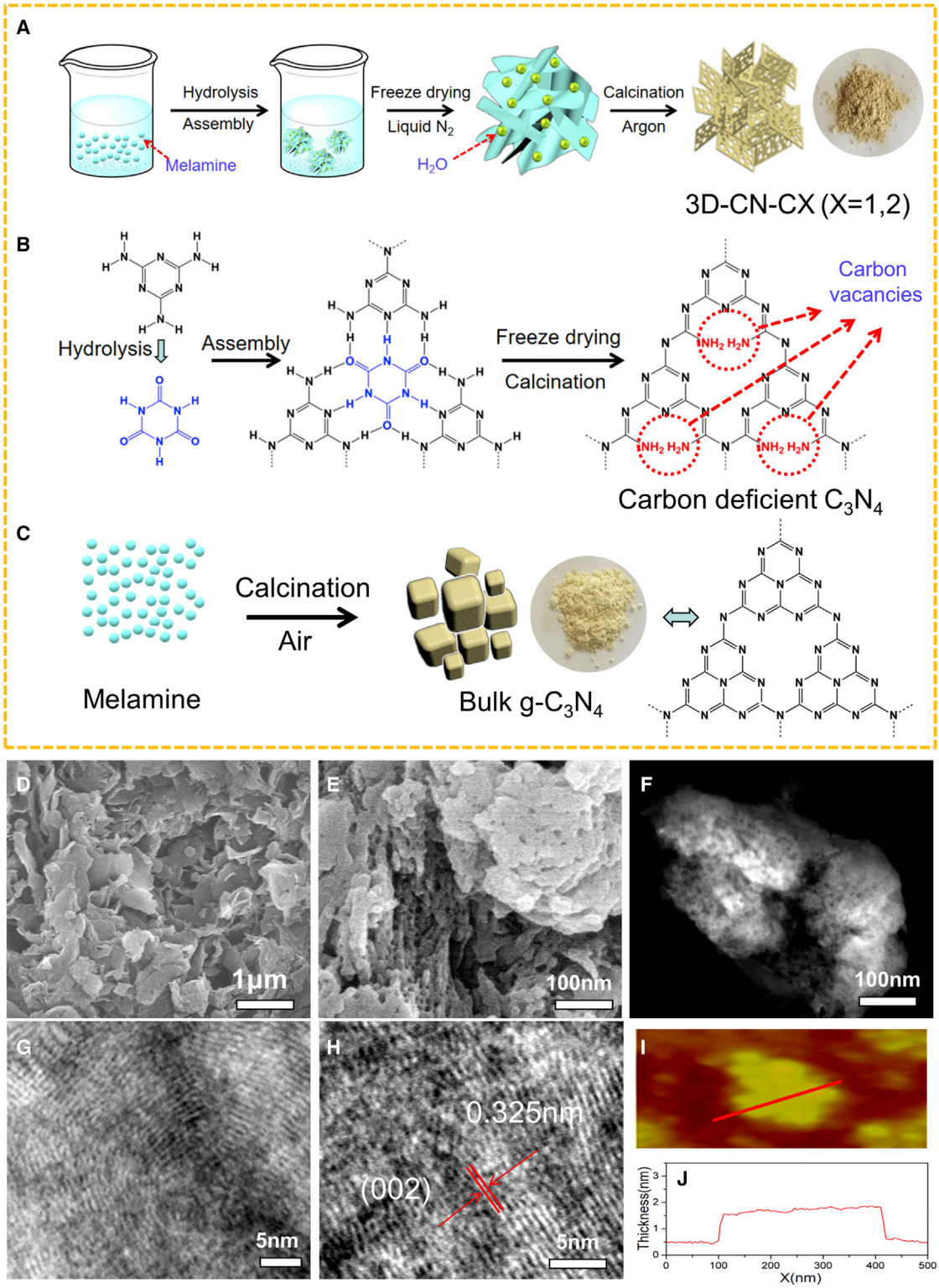

Figure 1. Schematic preparation process and morphology characterizations

(A–C) Schematic preparation process (A and B) of the 3D hierarchical porous carbon-deficient C_3N_4 architecture (3D-CN-C), as compared with (C) bulk C_3N_4 (B-CN) synthesis route.

(D–F) SEM images (D and E) and HAADF-TEM image (F) of the 3D-CN-C1 sample.

structure. For the synthesis, first the melamine powder (Figure S1A) was dissolved in water at 70°C, leading to the formation of cyanuric acid upon hydrolysis. Subsequently, cyanuric-acid-melamine supramolecular networks are generated through the hydrogen bonding interactions between melamine and cyanuric acid (Figure 1B). The resultant white supramolecular polymer precipitate (Figure S1B) was freeze-dried in liquid nitrogen to obtain a fluffy flaky material (Figure S1C) and then calcined. A three-dimensional (3D) hierarchical architecture made of assembled porous g-C_3N_4 nanoplatelets with abundant carbon vacancies is obtained (Figures 1A and 1B). The elimination of residual water molecules attached on the freeze-dried precursor generates carbon vacancies and mesoporosity into the framework of the g-C_3N_4 nanoplatelets upon calcination. Two-carbon-deficient 3D hierarchical porous g-C_3N_4 samples (3D-CN-CX, wherein X = 1, 2 assigns the calcination temperatures of 520°C and 550°C, respectively) were prepared. Bulk g-C_3N_4 (B-CN) was prepared as reference sample by direct calcination of melamine under air atmosphere (Figure 1C; refer to supplemental information for more details).

SEM analysis of the 3D-CN-C1 sample reveals a 3D porous framework, which is hierarchically assembled from ultrathin g-C_3N_4 nanoplatelets (Figure 1D). The nanoplatelets exhibit a curly shape with characteristic sizes below 1 μm and abundant mesopores in the 5–20 nm range (Figure 1E). The 3D-CN-C2 sample presents a similar structure (Figure S1D). In contrast, B-CN is made of irregular agglomerates of 0.2–2 μm in size (Figures S1E and S1F). The g-C_3N_4 nanosheets (NS-CN), prepared as a reference,[30] show a smooth surface and an average particle size of 1–3 μm (Figures S1G and S1H). The high-angle annular dark-field transmission electron microscopy (HAADF-TEM) images of 3D-CN-C1 (Figures 1F and S2) confirm the porous nature of the nanoplatelets as observed by SEM. Such 3D hierarchical porous structure is expected to provide more surface reactive sites and facile mass transfer for the surface reaction.[29,31,34] Integrated differential phase contrast scanning transmission electron microscopy (iDPC-STEM) enables obtaining images using a very low electron dose (below 600 e/A^2 in this case), ideal for imaging beam sensitive materials, such as ultrathin C_3N_4 nanoplatelets at high resolution.[36] iDPC-STEM images (Figures 1G and 1H) evidence the layered and corrugated structure of carbon-defective C_3N_4 nanoplatelets, with a measured d-spacing of 0.325 nm, like the (002) interplanar distance in pure phase C_3N_4. The atomic force microscopy (AFM) image (Figure 1I) indicates a nanoplatelet thickness of about 1.8 nm (Figure 1J), corresponding to about 4 g-C_3N_4 layers.[29] The X-ray powder diffraction (XRD) patterns of the as-prepared samples are shown in Figure S3A. All materials display the characteristic diffraction peaks of g-C_3N_4. For B-CN, the weak peak at 13.05° and the strong intense peak at 27.62° are attributed to the (100) in-plane structural packing motif and (002) interlayer stacking of aromatic segments, respectively.[22–24] The NS-CNs show a very similar XRD pattern to B-CN. Compared with B-CN, the (002) diffraction peak in 3D-CN-C1 is shifted from 27.62° to 27.70°, indicating a reduced interlayer distance. The significantly lower peak intensity is attributed to higher disorder (formation of carbon vacancies and mesoporosity) of the nanoplatelets assembled architecture of 3D-CN-C1. The further reduced peak intensity in 3D-CN-C2 is ascribed to the presence of higher amount of carbon vacancies. Solid-state ^{13}C and ^{1}H magic-angle spinning (MAS) NMR analyses provide further structural information about 3D-CN-C samples. As shown in Figure 2A, the ^{13}C nuclear magnetic resonance (NMR)

(G) iDPC-STEM image showing a stacked corrugated graphene-like structure.
(H) Magnified iDPC image showing an interplanar separation similar to the (002) spacing of the layers in the C_3N_4 graphene-like structure (P-6m2 space group).
(I and J) AFM image (I) and cross-section analysis (J) of the 3D-CN-C1 sample.

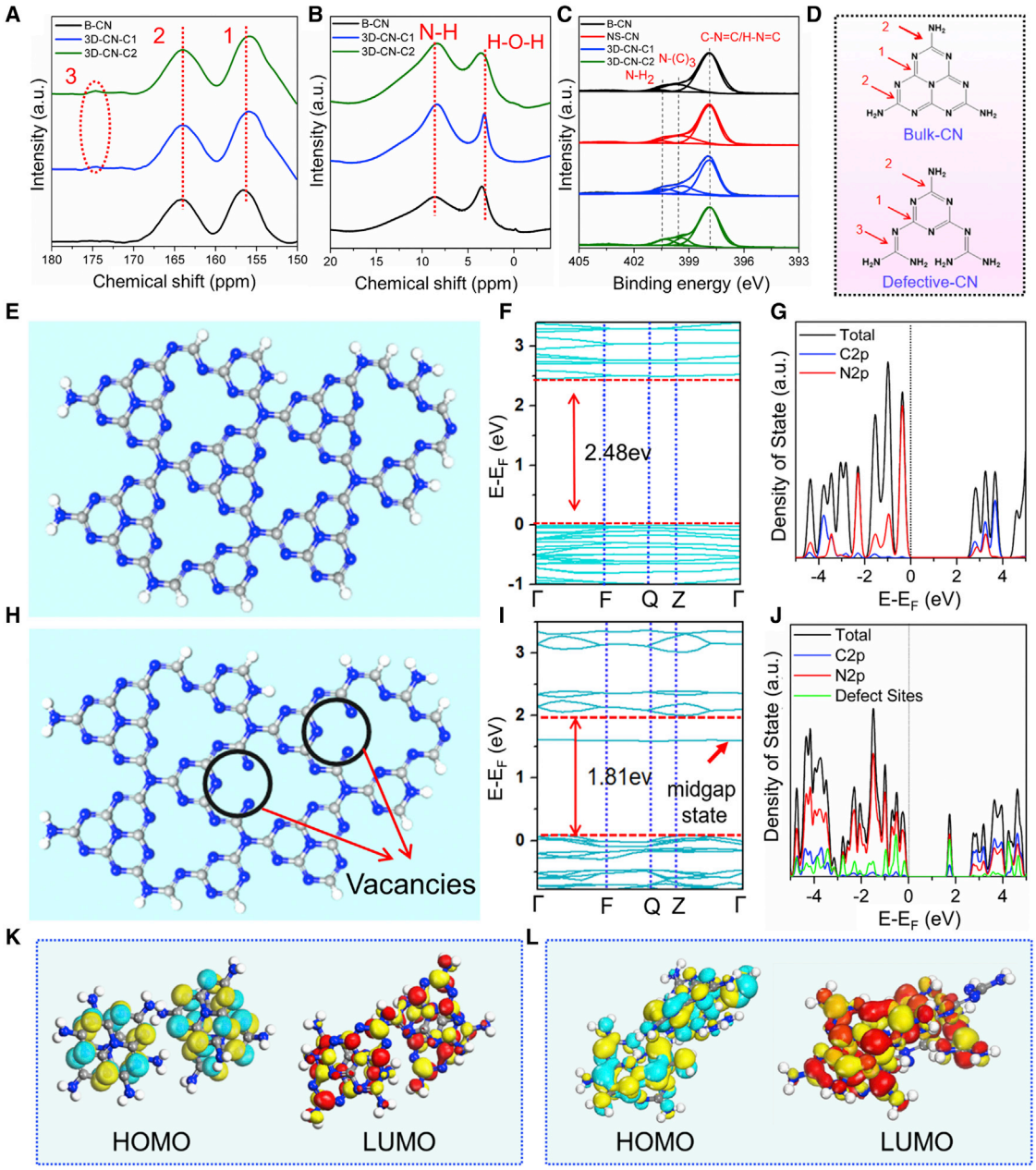

Figure 2. Structural characterizations and DFT calculations

(A–D) Solid-state ^{13}C (A) and ^{1}H MAS (magic angle spinning) (B) NMR spectra of bulk g-C_3N_4 and 3D-CN-C samples.

(C) High-resolution XPS spectra of N1s of the as-prepared samples.

(D) Proposed structures of bulk g-C_3N_4 and carbon-defective C_3N_4 building units.

(E–L) Detailed structures of (E) bulk-C_3N_4 (B-CN) and (H) carbon-defective C_3N_4 (3D-CN-C) frameworks as used for band structure calculations (C and N atoms are labeled in gray and blue, respectively), with the corresponding band gap and PDOS for B-CN (F and G) and 3D-CN-C1 (I and J), respectively. HOMO and LUMO spatial map of B-CN (K) and 3D-CN-C (L) samples.

spectra of B-CN, 3D-CN-C1, and 3D-CN-C2 samples exhibit two strong peaks at 156.2 and 164.3 ppm, corresponding to the chemical shifts of C_{3N} (signal 1) and $C_{2N\text{-}NHx}$ (signal 2) in the heptazine units.[19,21] The new peak, at 175.1 ppm, for both 3D-CN-C1 and 3D-CN-C2 samples, is attributed to the carbon atoms (signal 3) in the defective heptazine units.[26] The ^{1}H NMR spectra (Figure 2B) show two peaks

at 3.4 and 8.5 ppm, which correspond to the chemical shifts of adsorbed water and NH_x in the heptazine units, respectively.[19] Compared with B-CN, the stronger peaks at 8.5 ppm from both 3D-CN-C1 and 3D-CN-C2 indicate the presence of more NH_x groups in these two samples. To further clarify the origin of H atoms of the NH_x group in the defective heptazine units, a ^2H (D) isotope labeling experiment was conducted. The synthesis process was similar to the preparation of 3D-CN-C1, except that H_2O was replaced by D_2O. The obtained sample, labeled as D-3D-CN-C1, was also analyzed by solid-state ^1H MAS NMR spectroscopy. The highly similar ^1H MAS NMR spectra between 3D-CN-C1 and D-3D-CN-C1 (Figure S4) indicate that H atoms comprising the carbon-defective heptazine units originate from the melamine precursor rather than from D_2O. The Fourier transform infrared (FT-IR) spectra are shown in Figure S3B. For all the samples, the broad peaks between 3000 and 3400 cm^{-1} belong to the N-H stretching vibration and the O-H band. The peaks in the 1100–1700 cm^{-1} region are attributed to sp2 C=N stretching vibration modes and the aromatic sp3 C-N bonds, whereas the intense peak at 810 cm^{-1} corresponds to the signature of the formation of tri-*s*-triazine.[15,20] The N-H stretching vibration in 3D-CN-C is much stronger than that of B-CN and NS-CN, suggesting that the formation of carbon vacancies breaks the N-C=N/H-C=N groups and more N-H bonds are generated.[24] These results are in good agreement with the NMR observations.

The C/N ratio and chemical bonding nature were further analyzed with XPS and elemental analysis (Figures 2C, S5, and Table S1). The surface C/N atomic ratio decreases from 0.76 to 0.78 for B-CN and NS-CN to 0.70 and 0.65 for 3D-CN-C1 and 3D-CN-C2, respectively. This further confirms that the carbon vacancies are generated in the 3D-CN-C samples and that a higher calcination temperature leads to more carbon vacancies. From the elemental analysis (Table S1), the carbon vacancy percentage for 3D-CN-C1 and 3D-CN-C2 is calculated to be around 10% and 15%, respectively. To further verify the formation of carbon vacancies in the samples, high-resolution XPS spectra of C 1s and N 1s of all the samples were acquired and analyzed. As shown in Figure S5B, the peaks at 284.1 and 287.5 eV are attributed to C-C bonds and $C\text{-}N_3$ bonds, respectively,[15,16] whereas the peaks at 397.9, 399.6, and 400.4 eV in the high-resolution N 1s spectra (Figure 2C) belong to C-N=C/H-N=C, $N\text{-}(C)_3$, and $C\text{-}NH_2$, respectively.[23–25] Table S1 summarizes the relative ratios of C-N=C/H-N=C, $N\text{-}(C)_3$ and $C\text{-}NH_2$ calculated from the N 1s spectra. Compared with B-CN, the peak area ratios of $N\text{-}(C)_3$ in 3D-CN-C1 and 3D-CN-C2 samples obviously are reduced, suggesting that the loss of carbon has its origins from the $N\text{-}(C)_3$ sites. The enhanced peak area ratio of $N\text{-}H_2$ in both deficient samples illustrates that the $N\text{-}(C)_3$ has been selectively converted into $N\text{-}H_2$ groups. The removal of tertiary carbon leads to the formation of N-H bonds, this mechanism being in good agreement with the NMR, FT-IR, and XPS analysis. Based on this physicochemical rationale, a structure for B-CN and carbon-defective 3D hierarchical porous g-C_3N_4 (3D-CN-C) is proposed (Figure 2D). Electron paramagnetic resonance (EPR) measurements in the dark of all the samples (Figure S6) show a single narrow line (~5 gauss) at $g \approx 2.003$. Such a signal has been estimated to the paramagnetic centers related to electrons delocalized in the conduction band[26] or carbon-centered radicals.[24] The concentration of paramagnetic centers in these samples is calculated to be very low in the ppm range.

Textural properties

The textural properties are assessed by N_2 adsorption-desorption analysis. As shown in Figure S7A, all the samples exhibit a type IV isotherm, with a hysteresis at high relative pressure p/p_o.[29,31,34] Benefiting from the 3D hierarchical porous framework assembled by numerous nanoplatelets, 3D-CN-C1 exhibits a quite large

specific surface area of 78.8 m^2 g^{-1}, which is approximately 6.2 times higher than that of B-CN (12.8 m^2 g^{-1}). The further increased specific surface area (86.9 m^2 g^{-1}) of 3D-CN-C2 can be attributed to the formation of more mesopores in the nanoplatelets by a higher calcination temperature. The NS-CN sample has a surface area of 99.7 m^2 g^{-1} (Table S1). Compared with B-CN and NS-CN, the much wider pore size distributions (2–30 nm) for 3D-CN-C1 and 3D-CN-C2 (Figure S7B) indicate that the novel HFDT method is beneficial for the formation of supplementary mesopores, thus improving the mass transportation.[31,34] The sharp N_2 adsorption uptake at high p/p_o of isotherms suggests the presence of interparticular macroporosity, confirming hierarchical porosity in NS-CN and 3D-CN-CX samples.

Optical and electronic properties

The photographs of as-prepared samples are shown in Figure S8A. Two 3D-CN-C samples exhibit much deeper color than B-CN and NS-CN, demonstrating their improved solar-light harvesting upon the introduction of carbon vacancies.[24] UV/visible absorption spectra (Figure S8B) demonstrate that the absorption edge of two 3D-CN-C samples shifts to longer wavelength in the visible region, being consistent with its brown-colored appearance. It is noteworthy that these two samples show an obvious tail absorption (about 660 nm) in the visible range, which is induced by the additional electronic states located within the intrinsic band gap of the semiconductor. The additional electronic states are also well known as mid-gap states generally derived from lattice vacancies or dopants.[20,21] A Tauc plot of 3D-CN-C1 is shown in Figure S8C. The mid-gap state induced energy gap is calculated to be 1.77 eV, which is much narrower than the band gaps (Eg = 2.52 and 2.5 eV) of B-CN and NS-CNs, respectively. Due to the energy difference between the mid-gap state and the intrinsic gap state, the photoinduced carriers in 3D-CN-C1 can spontaneously transfer between these two band gaps under visible-light irradiation, which can significantly enhance the separation efficiency of photoinduced carriers and subsequently promote the photocatalytic activity of 3D-CN-C1.[22] Compared with 3D-CN-C1, the dark brown 3D-CN-C2 exhibits an even higher absorption in the visible region due to the generation of more carbon vacancies.[12,13]

Density-functional theory (DFT) calculations of the band structure and partial density of states (PDOS) for B-CN and 3D-CN-C were conducted to establish the intrinsic relationship between carbon vacancies and the decreased band gap values. For 3D-CN-C1/2 samples, the carbon vacancy percentages are set on the basis of elemental analysis results to 10% and 15%, respectively. The extended model structures of B-CN and 3D-CN-C are shown in Figures 2E and 2H, respectively. With the introduction of carbon vacancies into the heptazine units of C_3N_4, the band gap value of 3D-CN-C1 is significantly reduced from 2.48 eV (B-CN) to 1.81 eV (Figures 2F and 2I), being in good agreement with the Tauc plots (Figure S8C) and the tail absorption around 660 nm in Figure S8B. For B-CN, both C 2p and N 2p orbitals contribute to the conduction band (CB), while the valence band (VB) mainly consists of N 2p orbitals (Figure 2G).[35] The band structure NS-CN is similar to that of B-CN because there are no carbon vacancies in both samples. The DOS of 3D-CN-C1 shows that the CB is mainly dominated by the C2p and N2p orbitals, and the VB is composed of the N 2p orbitals and to a lesser extent of C2p and defect site orbitals (Figure 2J).[26] Importantly, a defect induced mid-gap energy level appears approximately 1.48 eV above the valance band (Figure 2I), thus promoting photoinduced carriers separation in 3D-CN-C1 sample.[22,27] These results demonstrate that the significantly reduced band gap of 3D-CN-C1 compared with that of B-CN and NS-CN is due to the existence of carbon vacancies in the heptazine units.[24] The calculated band structure and corresponding PDOS for 3D-CN-C2

sample are illustrated in Figures S9A and S9B, showing that a further decrease in the band gap is achieved and a defect energy level at 0.9 eV is generated given the higher amount of carbon vacancies. Figure 2K confirms that the highest occupied molecular orbital (HOMO) and lowest unoccupied molecular orbital (LUMO) locations of g-C_3N_4 (B-CN) are uniformly delocalized over the heptazine rings, given the high symmetry of the planar structure in the g-C_3N_4 framework.[26,27] Conversely, the charge density is redistributed with electron-rich areas in 3D-CN-C1 (Figure 2L). Such localized charge accumulation is ascribed to the defect-related mid-gap states in C_3N_4, which prohibits the recombination of charge carriers and favors an enhanced photocatalytic activity.[21,24] Furthermore, electron density difference (EDD) plots (Figures S9C and S9D) show the enrichment of electron density at the uncoordinated N atom sites, hence favoring for photoreduction.

Photoelectrochemical characterization and photocatalytic performance

The photocurrent response is a direct indication of the photoinduced carriers separation rate in a material.[37,38] The 3D-CN-C1 sample presents a much higher photocurrent response than the B-CN and NS-CN reference sample, indicating that the introduction of carbon vacancies significantly favors the electron-hole pair separation (Figure 3A). For the 3D-CN-C2 sample, the photocurrent response is also higher than that of reference samples, with, however, an attenuated photocurrent response as compared with 3D-CN-C1, attributed to a reduced charge carrier mobility at higher vacancy density. With higher vacancy concentration, the average distance between the trapping sites becomes small, increasing the recombination probability of electron-hole pairs[39] indicating the importance of well-controlled carbon vacancy concentration. The excitonic states were also analyzed by photoluminescence (PL) measurements and as shown in Figure 3B. Generally, both the radiative transition and non-radiative transition are existed during the excited electrons transfer from the high energy level to low energy level.[40,41] For the radiative transition, the PL is presented because of the electrons transition from the excited state to the ground state. Differently, no PL is formed due to the vibrational relaxation process of electrons in the non-radiative transition process. In our case, the 3D-CN-C1 and 3D-CN-C2 exhibit drastically lower PL emission intensities in comparison with B-CN and NS-CN. This demonstrates that the non-radiative recombination of electrons and holes is the main decay process in the two deficient samples, and the radiative recombination is the main decay process in B-CN and NS-CN. The photocurrent response versus different monochromatic light illuminations (Figure 3C) shows again that 3D-CN-C1 exhibits a greatly enhanced current in both the visible and UV range, demonstrating augmented photocurrent and broadened photoresponse range. Additionally, the electrochemical impedance spectra (EIS) (Figure S10) illustrate the much smaller arc radius of the 3D-CN-C1 electrode, indicative of much faster electron transfer kinetics and surface reaction rate in the 3D-CN-C1 sample.[29]

The photocatalytic H_2O_2 production efficiency was studied with different reactants under visible-light irradiation (Figure 3D). Clearly, the 3D-CN-C1 sample presents the highest photocatalytic activity for H_2O_2 production, whichever reaction system was employed. In the "O_2 + isopropanol" system, the 3D-CN-C1 shows an unprecedentedly high H_2O_2 output of 251.5 μM (H_2O_2 evolution rate of 6287.5 μM g^{-1} h^{-1}), considerably higher than that of B-CN and NS-CN (4.2 and 1.6 times, respectively). Although the surface area of the NS-CN (99.7 m^2 g^{-1}) is larger than that of the 3D-CN-C1 (78.8 m^2 g^{-1}), the photocatalytic H_2O_2 production activity of the latter is significantly higher, which is related to the enhanced separation of the photoinduced carriers, increased visible-light harvesting, and utilization owing to carbon vacancies.[21,27] The 3D-CN-C1 sample exhibits a better performance than 3D-CN-C2

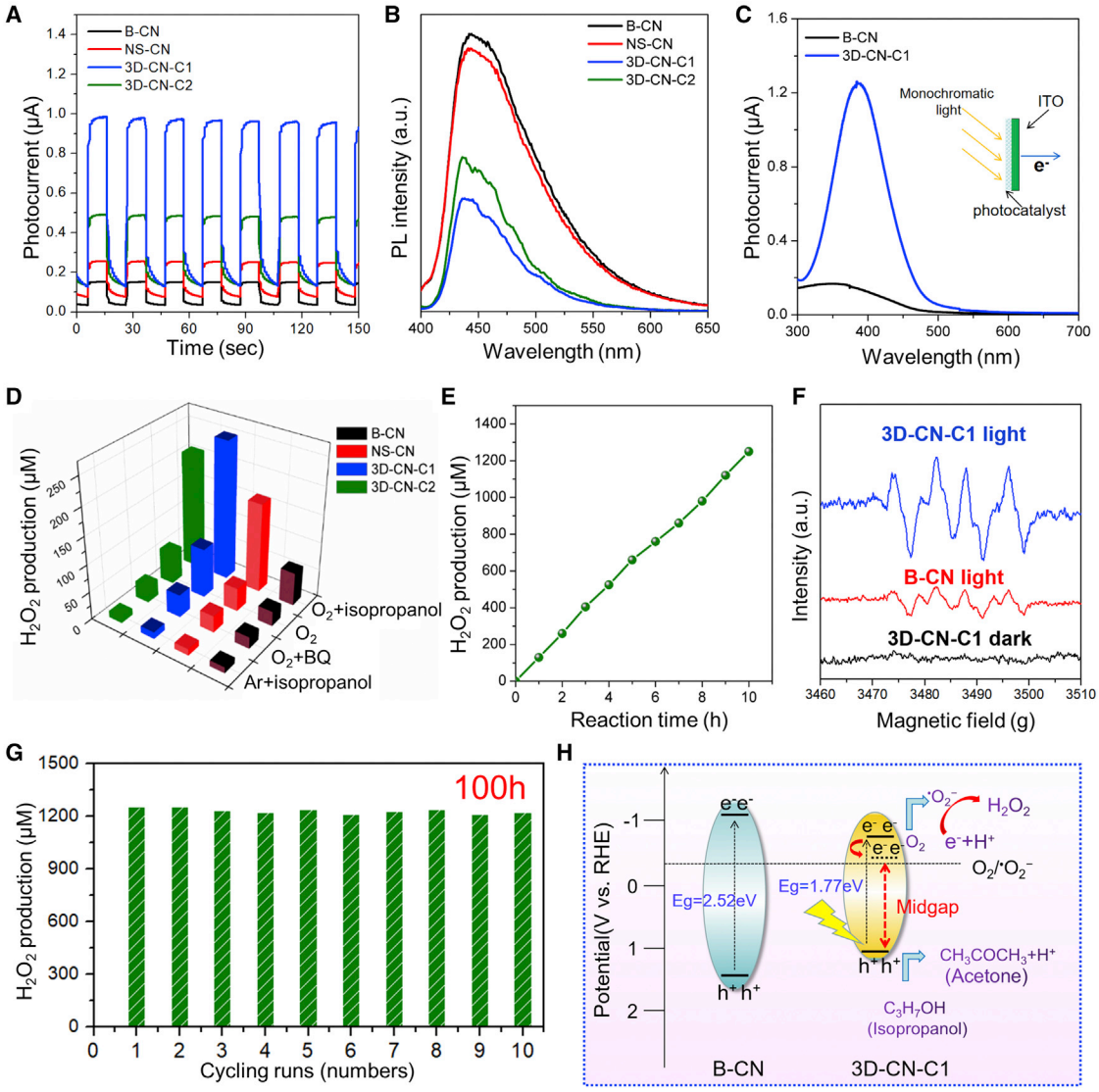

Figure 3. Photoelectrochemical characterizations and photocatalytic H_2O_2 production

(A and B) Transient photocurrent intensity (A) and PL spectra (B) of the as-prepared samples.

(C) Photocurrent response of B-CN and 3D-CN-C1 samples under various monochromatic light illuminations.

(D) Photocatalytic production rate of H_2O_2 with different additive agents under visible-light irradiation for 2 h for the as-prepared photocatalysts (photocatalyst loading of 20 mg in each reaction system).

(E) Time-dependent photocatalytic production of H_2O_2 by the 3D-CN-C1 sample in the O_2 + isopropanol system.

(F) ESR signals of DMPO-$^{\bullet}O_2^-$ for B-CN and 3D-CN-C1 under visible-light irradiation and dark condition.

(G) Cycling tests of the 3D-CN-C1 sample for H_2O_2 production.

(H) The proposed mechanism for photosynthetic H_2O_2 production in B-CN and 3D-CN-C1 samples in the O_2 + isopropanol reaction system.

owing to its better controlled carbon vacancy concentration, offering an excellent electron-hole separation rate. Contrast experiments were also carried out to explore the mechanism of the photocatalytic H_2O_2 production (Figure 3D). When the O_2 was replaced by Argon, all the samples exhibit negligible H_2O_2 production, revealing the vital role of O_2 in the H_2O_2 production. Compared with the O_2 + isopropanol system, eliminating the isopropanol leads to a lower photocatalytic H_2O_2 production. Although the 3D-CN-C1 sample still has the highest H_2O_2 production rate of 158 μM in a pure O_2 system, it is lower than that in the O_2 + isopropanol system, indicating that isopropanol acts as a sacrificial agent, which preferentially combines with

the photogenerated holes and facilitates the formation of a proton (H^+). Hence, the lower H_2O_2 production for all the as-prepared photocatalysts in the O_2 system (without isopropanol) is possibly originated from the combination of $^{\bullet}O_2^-$ and H^+ from water. The generation of $^{\bullet}O_2^-$ intermediate species during photocatalytic H_2O_2 production is revealed by the use of the ESR (electron spin resonance) technique (Figure 3F).[9] Again, the 3D-CN-C1 photocatalyst is found to give the higher intensity for DMPO-$^{\bullet}O_2^-$ signal, suggesting enhanced $^{\bullet}O_2^-$ formation capability of 3D-CN-C1.[27] No DMPO-$^{\bullet}O_2^-$ signal was found for 3D-CN-C1 photocatalyst under dark conditions, indicating the significant role of light for photoelectrons formation. To further understand the influence of $^{\bullet}O_2^-$ on the H_2O_2 production, 1,4-benzoquinone (BQ) was used as radical scavenger. All samples show a reduced H_2O_2 production in the "O_2 + BQ" system, which demonstrates the essential role of $^{\bullet}O_2^-$ intermediate in the H_2O_2 production process.[12,15] Ten consecutive photocatalytic H_2O_2 production runs with a total reaction time of 100 h (Figure 3G) were carried out. It is worth noting that each cycle extends to a very long reaction duration of 10 h, the longest cycle duration compared with those in the literature. Generally, the photocatalytic H_2O_2 production over C_3N_4-based materials suffers from unsatisfactory stability after long-term cycling due to the intrinsically decreased crystallinity and self-decomposition of H_2O_2 on the surface of photocatalysts. Inspiringly, the H_2O_2 production of our 3D-CN-C1 photocatalyst remains almost unchanged after a long-term cycling operation of 100 h, which is superior to that of C_3N_4-based photocatalysts reported in previous publications (Table S2). Combined with the fact that the H_2O_2 production of 3D-CN-C1 increases linearly as function of reaction time (Figure 3E), this indicates a stable and robust photocatalytic process and materials. The high efficiency and extraordinary stability for H_2O_2 production endow our 3D-CN-C1 photocatalyst with great potential in practical production and application. The XRD pattern and TEM image of the 3D-CN-C1 sample after use (Figure S11) additionally proves its excellent stability.[15] The H_2O_2 production rate of 6287.5 $\mu M\ g^{-1}\ h^{-1}$ by the 3D-CN-C1 sample under visible light is the best value and much higher than the values reported in literature (Table S2). Moreover, the consecutive cycling tests of the B-CN and NS-CN samples for H_2O_2 production were also conducted for ten cycles and presented in Figure S12. The stable input of H_2O_2 further indicates the merits of g-C_3N_4-based materials in photocatalytic H_2O_2 formations, and more studies should focus on this promising field in the future.[19–21] The photocatalytic H_2O_2 experiments over 3D-CN-1 photocatalyst under various monochromatic light illumination were conducted. As shown in Figure S13, there is almost no H_2O_2 formation when the wavelength of monochromatic light over 550 nm. Meanwhile, the wavelength-dependent H_2O_2 evolution matches well with photocurrent response curves (Figure 3C) rather than UV-visible (UV-vis) absorption spectrum (Figure S8B), indicating the crucial role of photoinduced charges separation in photocatalytic H_2O_2 evolution.[27,28] Although the 3D-CN-1 photocatalyst displays the stronger absorption over 550 nm, the photoinduced charge separation is still unsatisfactory, as verified by the photocurrent response curves, thus leading to the poor H_2O_2 evolution. The above results suggest that in addition to the enhanced light absorption, the formation and separation of photoinduced carriers are also essential for the photocatalytic process.[33,38]

Photocatalytic mechanism and theoretical simulations

Based on the structural and catalytic analyses, a mechanism for the photosynthetic H_2O_2 production is proposed (Figure 3H). The reduced band gap, as determined from XPS VB spectra (Figure S14) and Tauc plots (Figure S8C),[26,31] combined with the 3D hierarchical porous architecture of 3D-CN-C, is favorable for visible-light absorption. Moreover, the formed mid-gap states in 3D-CN-C facilitate the

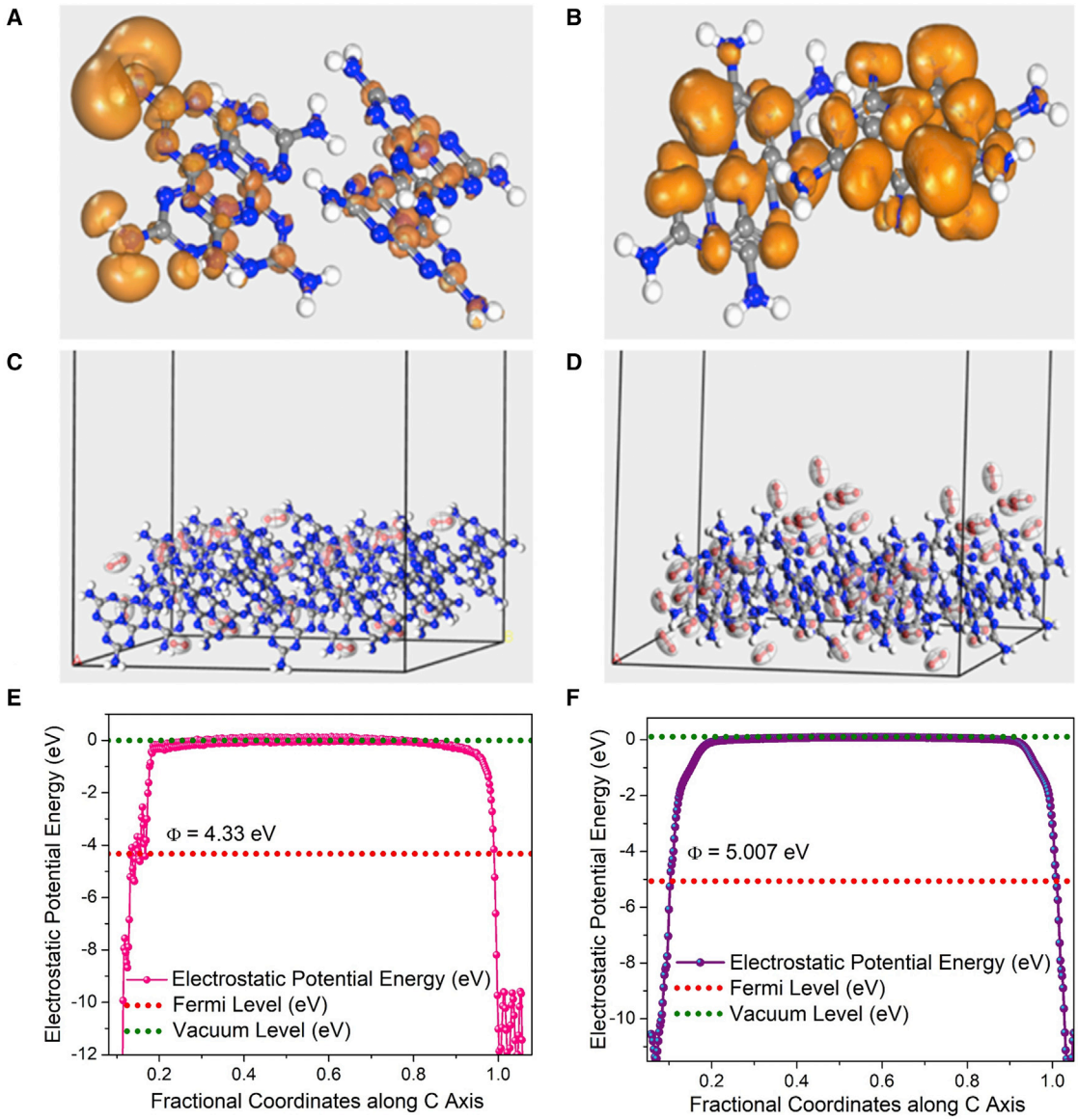

Figure 4. Theoretical simulations and calculations

(A and B) Fukui function (FF) plots for favored radical attack site for (A) B-CN and (B) 3D-CN-C.

(C and D) $^{\bullet}O_2^-$ adsorption simulations for (C) B-CN and (D) 3D-CN-C.

(E and F) Electrostatic potential plots for (E) B-CN and (F) 3D-CN-C.

electron-hole transfer and separation under visible-light illumination.[19,24] The holes are trapped by isopropanol to generate acetone and protons (H^+). Besides, the accumulated electrons in the 3D-CN-C CB are easily captured by O_2, generating $^{\bullet}O_2^-$, given that the energy level of the CB in 3D-CN-C is lower than that of $O_2/^{\bullet}O_2^-$ redox couple (−0.33 eV vs RHE). H_2O_2 is finally produced due to the further reduction of $^{\bullet}O_2^-$. The detailed route of the photosynthetic H_2O_2 production process is presented and discussed from Data S1 (supplemental information).

FF simulations were additionally carried out to reveal the role of carbon vacancies in the photocatalytic H_2O_2 production process.[42] The Fukui charge values of various N sites are displayed in Figure S15. Compared with the FF plot of B-CN (Figure 4A), the

3D-CN-C sample shows a very high degree of active sites favoring radical attack (Figure 4B). The N atoms in the carbon-defective triazine ring present a very large degree of affinity toward a radical attack, which is essential toward high yield of H_2O_2 production. Adsorption simulations[43] show that 3D-CN-C1 (Figure 4D) demonstrates a very high extent of $^{\bullet}O_2^-$ radical loading compared with B-CN, wherein the adsorption of $^{\bullet}O_2^-$ radicals is through a weak H bonding with H atoms linked with the C and N atoms in the triazine ring (Figure 4C). The drastically increased affinity for the $^{\bullet}O_2^-$ radicals in cases of 3D-CN-C1 as a significant accumulation of $^{\bullet}O_2^-$ species is observed around the carbon vacancies from the HOMO-LUMO and FF simulations, which is favorable for H_2O_2 production. Electrostatic potential energy plots are shown in Figures 4E and 4F for B-CN and 3D-CN-C1, respectively. The work function value of 3D-CN-C1 is 5.007 eV, considerably larger than 4.33 eV of B-CN. The higher work function of 3D-CN-C1 suggests its stronger electron affinity in favor of $^{\bullet}O_2^-$ radicals formation.[44,45] The Fermi level value in 3D-CN-C samples also shifts to more negative values compared with B-CN, indicating the formation of higher band bending and charge injection for 3D-CN-C1, and provides a high driving force for photoreduction.[46] All these results demonstrate that carbon vacancies have strong electron affinity and promote the generation of $^{\bullet}O_2^-$ radicals that are responsible for the unprecedented photocatalytic H_2O_2 production performance, and a better modulation of their concentration is essential.

In summary, a significantly enhanced photocatalytic H_2O_2 production with an extraordinary stability is achieved by a novel carbon-deficient 3D hierarchical porous g-C_3N_4 scaffold prepared by an innovative HFDT process. The carbon vacancies in the C_3N_4 lattice are found to decrease the band gap and generate mid-gap electronic levels, broadening the visible-light absorption and facilitating the photoinduced carrier separation. The ESR spin-trap experiments confirm the essential role of intermediate $^{\bullet}O_2^-$ radical species during photocatalytic H_2O_2 production. The carbon vacancies show a very strong affinity for electrons and $^{\bullet}O_2^-$ radicals, and their accumulation in close proximity of the active sites favors the $^{\bullet}O_2^-$ reduction, boosting H_2O_2 production. On the other hand, the unique 3D hierarchical porous g-C_3N_4 structure, with a larger specific surface area and abundant pores, provides numerous reactive centers and a convenient pathway for the transport of reactants and products. Our photocatalyst with a well-controlled carbon vacancy concentration demonstrates an H_2O_2 output of 6287.5 $\mu M\ g^{-1}\ h^{-1}$ under visible-light irradiation with an outstanding long cycling stability, being the best value achieved to date when compared with other similar reported photocatalysts in literature. This work offers highly efficient photocatalysts suitable for a safe and environmentally friendly large-scale industrial production of H_2O_2.

EXPERIMENTAL PROCEDURES

Resource availability

Lead contact

Further information and requests for resources should be directed to and will be fulfilled by the lead contact, Bao-Lian Su (bao-lian.su@unamur.be).

Materials availability

This study did not generate new unique reagents.

Data and code availability

All data related to this study included in the article and supplemental information will be provided by the lead contact upon request.

Materials

Potassium iodide, sodium sulfate, ammonium molybdate tetrahydrate, and Nafion were purchased from Merck and melamine from Aladdin and used without further purification. Distilled water was used in the whole experiment process.

Synthesis of 3D-CN-C, bulk g-C_3N_4 (B-CN), and C_3N_4 nanosheets (NS-CN)

For the synthesis of an innovative carbon-deficient 3D porous g-C_3N_4, a novel HFDT of melamine was developed. In a typical synthesis, 2 g of melamine was dissolved in 50 mL of deionized water with stirring for 2 h at 70°C. The obtained solution was filtered to remove the solid residues, and the filtrate was naturally let to cool down at room temperature. A white flocculent solid of hydrated melamine was obtained. The liquid nitrogen was used to freeze-dry the flocculent solid. Finally, the freeze-dried product was heated at 520°C for 4 h in an Ar atmosphere to obtain a 3D-CN-C1 sample, whereas a 3D-CN-C2 sample was prepared by calcinating the freeze-dried precursor at 550°C for 4 h in an Ar atmosphere. The schematic preparation process of the 3D-CN-C sample is illustrated in Figures 1A and 1B. B-CN was synthesized by direct calcination of melamine powder in a muffle furnace at 550 °C for 4 h. NS-CNs were prepared according to the literature.[30]

Characterizations

X-ray diffraction (XRD) patterns were obtained on a Bruker D8 system with Cu Ka radiation (λ = 0.15405 nm), with a scanning rate of 4°/min and range within 10°–50°. The ^{13}C and ^{1}H solid-state MAS NMR measurements were conducted on a Bruker Avance 500 MHz (7 T) spectrometer using 4 mm zirconia rotors as sample holders, with a spinning rate of 10 kHz. Elemental analysis (C, H, and N) was performed on a vario EL microanalyzer. Scanning electron microscopy (SEM) observation was carried out using JEOL 7500F field-emission SEM. TEM images were acquired on polymer coated copper grids by using a Tecnai 10 apparatus. Atomic force microscopy (AFM) imaging was performed on a Park XE70 AFM (Park Systems, Korea). Nitrogen adsorption-desorption isotherms were recorded using an ASAP 2420 surface area and porosity analyzer at 77 K. The specific surface area was calculated by the Brunauer-Emmett-Teller (BET) method. The pore size distribution was calculated by the Barrett-Joyner-Halenda (BJH) method and non-local density-functional theory (NLDFT) analysis method. X-ray photoelectron spectroscopy (XPS) analysis was performed on a Thermo Fisher ESCALAB 250Xi instrument with a monochromatic Al Kα X-ray source (1486.6 eV). The EPR spectra on dry powders were recorded on a Varian E-line spectrometer with a standard rectangular cavity (TE102 mode), an HP 5342A microwave frequency counter, and a Bruker NMR ER 035 M Gaussmeter, using diphenyl picrylhydrazyl (DPPH; g = 2.0036) for field calibration. The static magnetic field was modulated at 10 kHz with an amplitude of 1.6 gauss. To avoid saturation, spectra had to be recorded at low microwave power (60 μW). The ESR signals of free radicals were examined by using 5,5-dimethyl-L-pyrroline N-oxide (DMPO) as a probe on a Bruker ER200-SRC spectrometer under visible-light irradiation. The UV-vis absorption spectra were collected by a UV-vis spectrophotometer (Perkin Elmer Lambda 35 UV-vis spectrometer) in the wavelength range of 200–800 nm. PL properties of the samples were investigated by Perkin Elmer LS45 luminescence spectrophotometer.

Photocatalytic H_2O_2 production experiments

In a typical process, 20 mg of catalyst was dispersed in a mixture of water (19 mL) and isopropanol (1 mL). The solution was bubbled with O_2 for 10 min to saturation. Before the light irradiation, the solution was put in a dark box and magnetically stirred for 30 min to reach an adsorption-desorption equilibrium. Afterward, the

photocatalytic reaction was carried out under visible-light irradiation (400–800 nm) by using 6 neon lamps of 20 W at room temperature for 2 h. Finally, 2 mL of solution was taken from the beaker and immediately centrifuged for the separation of photocatalyst for analyses. For the comparative experiments, the solution was bubbled with Ar instead of O_2 for 10 min before measurement. The amount of H_2O_2 was analyzed by conventional iodometry method, as reported in literature.[16] In brief, 1 mL of 0.1 mol L^{-1} ammonium molybdate tetrahydrate aqueous solution and 1 mL of 0.4 mol L^{-1} potassium iodide (KI) aqueous solution were added to the obtained 2 mL of filtrate, which was then kept for 1 min. The H_2O_2 molecules reacted with iodide anions (I^-) under acidic conditions to produce I_3^- anions, which possess a strong absorption at around 350 nm. The amount of I_3^- was analyzed by the UV-vis spectroscopy test and the amount of H_2O_2 was consequently calculated. The photocatalytic H_2O_2 generation under various monochromatic light illumination were conducted by setting the input of specific wavelength on the computer-controlled electrochemical workstation (CHI 660E) with a xenon arc lamp.[34,35]

Photoelectrochemical measurements

The photoelectrochemical measurements were conducted in a typical three-electrode cell by using the computer-controlled electrochemical workstation (CHI 660E).[34,35] Typically, 20 mg of catalyst sample was added into a mixed solution of deionized water (100 μL) and Nafion (50 μL). After ultrasonic treatment for 10 min, the prepared homogeneous suspension (50 μL) was uniformly sprayed onto the surface of indium tin oxide (ITO) (1.0 × 1.0 cm). The ITO glass with photocatalyst served as the working electrode, whereas a Pt plate and a saturated calomel electrode (SCE) were used as the counter and the reference electrode, respectively. A 0.1 M Na_2SO_4 solution was used as the electrolyte, and the visible light was supplied by a xenon arc lamp PLS-SXE-300C with a 420 nm cutoff filter. The photocurrent-time (I-t) curves were collected at the open-circuit potential. EIS test was carried out in a 0.2 M KCl solution. The collected potentials versus SCE electrode were converted to the reversible hydrogen electrode (RHE) according to the following formula: E (RHE) = 0.242 + 0.059 pH + E (SCE).[35]

Computational details

DFT calculations have been performed using the generalized gradient approximation (GGA) functional with Perdew-Burke-Ernzerhof (PBE) exchange correlation and ultrasoft type pseudopotentials with Koelling-Harmon relativistic treatment and Gimme parameters to account for DFT-D (van der Walls) correction. Band structure and DOS calculations were carried out using CASTEP code using a (2 × 2 × 2) supercell (Figure S16). A. Monkhorst Pack Scheme (5 × 5 × 1) k-point mesh was taken. Plane wave cutoff was set at 570 eV. Self-consistent field (SCF) cutoff was set at 1×10^{-6} eV. Geometry optimization was carried out prior to DFT calculations with energy cutoff set at 1×10^{-7} eV, with maximum force set at 0.01 eV/Å. HOMO, LUMO, EDD, and FF calculations were performed using Dmol3 code using an H-terminated nonperiodic C_3N_4 structure using B3LYP functional with double numerical plus d-function (DND) basis set and basis file 3.5. SCF tolerance was set at 1×10^{-6} eV, and geometry optimization was carried out prior to calculations with energy cutoff set at 1×10^{-7} eV, with maximum force set at 0.004 eV/Å. Adsorption calculations were carried out using Monte Carlo simulations with Ewald electrostatic attractions using the Metropolis method and atom-based van der Walls interactions with COMPASS II force field in SORPTION code.

SUPPLEMENTAL INFORMATION

Supplemental information can be found online at https://doi.org/10.1016/j.xcrp.2022.100874.

ACKNOWLEDGMENTS

Y.D. thanks the China Scholarship Council (201808310127) for financial support. This work is financially supported by the National Natural Science Foundation of China (U1663225), Program for Changjiang Scholars and Innovative Research Team in University (IRT_15R52) of the Chinese Ministry of Education, Program of Introducing Talents of Discipline to Universities-Plan 111 (grant no. B20002) from the Ministry of Science and Technology and the Ministry of Education of China, and the National Key R&D Program of China (2016YFA0202602). This research was also supported by the European Commission Interreg V France-Wallonie-Vlaanderen project "DepollutAir".

AUTHOR CONTRIBUTIONS

Y.D. carried out all experiments and wrote the paper, and T.B. helped the realization of the experiments. S.M. and S.R. conducted the DFT calculations. D.A.E., S.B., and G.V.T conducted the HAADF-TEM and iDPC-STEM characterizations. H.V. carried out the EPR analysis. J.L, A.V., and Y.L. took part in the establishment of research project. All the authors discussed the results and verified and revised the paper. Y.L. helped to finalize the manuscript. B.-L.S. established the research direction, conceived the project, provided the scientific guidance and project realization ideas, and revised and finalized the paper.

DECLARATION OF INTERESTS

The authors declare no competing interests.

Received: February 9, 2022
Revised: March 23, 2022
Accepted: April 7, 2022
Published: April 28, 2022

REFERENCES

1. Chen, L., Wang, L., Wan, Y., Zhang, Y., Qi, Z., Wu, X., and Xu, H. (2020). Acetylene and diacetylene functionalized covalent triazine frameworks as metal-free photocatalysts for hydrogen peroxide production: a new two-electron water oxidation pathway. Adv. Mater. *32*, 1904433.

2. Hirakawa, H., Shiota, S., Shiraishi, Y., Sakamoto, H., Ichikawa, S., and Hirai, T. (2016). Au nanoparticles supported on $BiVO_4$: effective inorganic photocatalysts for H_2O_2 production from water and O_2 under visible light. ACS Catal. *6*, 4976–4982.

3. Kofuji, Y., Isobe, Y., Shiraishi, Y., Sakamoto, H., Tanaka, S., Ichikawa, S., and Hirai, T. (2016). Carbon nitride-aromatic diimide–graphene nanohybrids: metal-free photocatalysts for solar-to-hydrogen peroxide energy conversion with 0.2% efficiency. J. Am. Chem. Soc. *138*, 10019–10025.

4. Cai, J., Huang, J., Wang, S., Iocozzia, J., Sun, Z., Sun, J., Yang, Y., Lai, Y., and Lin, Z. (2019). Crafting mussel-inspired metal nanoparticle-decorated ultrathin graphitic carbon nitride for the degradation of chemical pollutants and production of chemical resources. Adv. Mater. *31*, 1806314.

5. Shiraishi, Y., Kofuji, Y., Sakamoto, H., Tanaka, S., Ichikawa, S., and Hirai, T. (2015). Effects of surface defects on photocatalytic h_2o_2 production by mesoporous graphitic carbon nitride under visible light irradiation. ACS Catal. *5*, 3058–3066.

6. Teranishi, M., Hoshino, R., Naya, S.I., and Tada, H. (2016). Gold-nanoparticle-loaded carbonate-modified titanium (IV) oxide surface: visible-light-driven formation of hydrogen peroxide from oxygen. Angew. Chem. Int. Ed. *55*, 12773–12777.

7. Zhang, P., Tong, Y., Liu, Y., Vequizo, J.J.M., Sun, H., Yang, C., Yamakata, A., Fan, F., Lin, W., Wang, X., et al. (2020). Heteroatom dopants promote two-electron O_2 reduction for photocatalytic production of H_2O_2 on polymeric carbon nitride. Angew. Chem. Int. Ed. *59*, 16209–16217.

8. Tsukamoto, D., Shiro, A., Shiraishi, Y., Sugano, Y., Ichikawa, S., Tanaka, S., and Hirai, T. (2012). Photocatalytic H_2O_2 production from ethanol/O_2 system using TiO_2 loaded with Au-Ag bimetallic alloy nanoparticles. ACS Catal. *2*, 599–603.

9. Hou, H., Zeng, X., and Zhang, X. (2020). Production of hydrogen peroxide by photocatalytic processes. Angew. Chem. Int. Ed. *59*, 17356–17376.

10. Shiraishi, Y., Kanazawa, S., Kofuji, Y., Sakamoto, H., Ichikawa, S., Tanaka, S., and Hirai, T. (2014). Sunlight-driven hydrogen peroxide production from water and molecular oxygen by metal-free photocatalysts. Angew. Chem. Int. Ed. *53*, 13454–13459.

11. Yang, L., Chen, H., Xu, Y., Qian, R., Chen, Q., and Fang, Y. (2022). Synergetic effects by Co^{2+} and PO_4^{3-} on Mo-doped $BiVO_4$ for an improved photoanodic H_2O_2 evolution. Chem. Eng. Sci. *251*, 117435.

12. Fang, Y., Hou, Y., Fu, X., and Wang, X. (2022). Semiconducting polymers for oxygen evolution reaction under light illumination. Chem. Rev. *122*, 4204–4256.

13. Peng, Y., Zhou, L., Wang, L., Lei, J., Liu, Y., Daniele, S., and Zhang, J. (2019). Preparation of NiCoP-decorated g-C_3N_4 as an efficient photocatalyst for H_2O_2 production. Res. Chem. Intermediat. *45*, 5907–5917.

14. Isaka, Y., Kawase, Y., Kuwahara, Y., Mori, K., and Yamashita, H. (2019). Two-phase system utilizing hydrophobic metal-organic frameworks (MOFs) for photocatalytic synthesis of hydrogen peroxide. Angew. Chem. Int. Ed. *58*, 5402–5406.

15. Wei, Z., Liu, M., Zhang, Z., Yao, W., Tan, H., and Zhu, Y. (2018). Efficient visible-light-driven selective oxygen reduction to hydrogen peroxide by oxygen-enriched graphitic carbon

nitride polymers. Energ. Environ. Sci. *11*, 2581–2589.

16. Lei, J., Chen, B., Lv, W., Zhou, L., Wang, L., Liu, Y., and Zhang, J. (2019). Robust photocatalytic H_2O_2 production over inverse Opal g-C_3N_4 with carbon vacancy under visible light. ACS Sustain. Chem. Eng. *7*, 16467–16473.

17. Kim, H.I., Kwon, O.S., Kim, S., Choi, W., and Kim, J.H. (2016). Harnessing low energy photons (635 nm) for the production of H_2O_2 using upconversion nanohybrid photocatalysts. Energ. Environ. Sci. *9*, 1063–1073.

18. Moon, G.H., Kim, W., Bokare, A.D., Sung, N.E., and Choi, W. (2014). Solar production of H_2O_2 on reduced graphene oxide-TiO_2 hybrid photocatalysts consisting of earth-abundant elements only. Energ. Environ. Sci. *7*, 4023–4028.

19. Zhao, Q., Fu, L., Jiang, D., Xi, Y., and Yang, H. (2018). A nanoclay-induced defective g-C_3N_4 photocatalyst for highly efficient catalytic reactions. Chem. Commun. *54*, 8249–8252.

20. Lau, V.W.H., Yu, V.W.Z., Ehrat, F., Botari, T., Moudrakovski, I., Simon, T., Duppel, V., Medina, E., Stolarczyk, J., Feldmann, J., et al. (2017). Urea-modified carbon nitrides: enhancing photocatalytic hydrogen evolution by rational defect engineering. Adv. Energy Mater. *7*, 1602251.

21. Yu, H., Shi, R., Zhao, Y., Bian, T., Zhao, Y., Zhou, C., Waterhouse, G., Wu, L.-Z., Tung, C.-H., and Zhang, T. (2017). Alkali-assisted synthesis of nitrogen deficient graphitic carbon nitride with tunable band structures for efficient visible-light-driven hydrogen evolution. Adv. Mater. *29*, 1605148.

22. Yang, P., Zhuzhang, H., Wang, R., Lin, W., and Wang, X. (2019). Carbon vacancies in a melon polymeric matrix promote photocatalytic carbon dioxide conversion. Angew. Chem. Int. Ed. *58*, 1134–1137.

23. Wang, W., Zhang, H., Zhang, S., Liu, Y., Wang, G., Sun, C., and Zhao, H. (2019). Potassium-ion-assisted regeneration of active cyano groups in carbon nitride nanoribbons: visible-light-driven photocatalytic nitrogen reduction. Angew. Chem. Int. Ed. *58*, 16644–16650.

24. Shi, L., Yang, L., Zhou, W., Liu, Y., Yin, L., Hai, X., Song, H., and Ye, J. (2018). Photoassisted construction of holey defective g-C_3N_4 photocatalysts for efficient visible-light-driven H_2O_2 production. Small *14*, 1703142.

25. Liu, D., Chen, D., Li, N., Xu, Q., Li, H., He, J., and Lu, J. (2020). Surface engineering of g-C_3N_4 by stacked BiOBr sheets rich in oxygen vacancies for boosting photocatalytic performance. Angew. Chem. Int. Ed. *59*, 4519–4524.

26. Zhao, D., Dong, C.L., Wang, B., Chen, C., Huang, Y.C., Diao, Z., Li, S., Guo, L., and Shen, S. (2019). Synergy of dopants and defects in graphitic carbon nitride with exceptionally modulated band structures for efficient photocatalytic oxygen evolution. Adv. Mater. *31*, 1903545.

27. Feng, C., Tang, L., Deng, Y., Wang, J., Luo, J., Liu, Y., Ouyang, X., Yang, H., Yu, J., and Wang, J. (2020). Synthesis of leaf-vein-like g-C_3N_4 with tunable band structures and charge transfer properties for selective photocatalytic H_2O_2 evolution. Adv. Funct. Mater. *30*, 2001922.

28. Teng, Z., Zhang, Q., Yang, H., Kato, K., Yang, W., Lu, Y.R., Liu, S., Wang, C., Yamakata, A., Su, C., et al. (2021). Atomically dispersed antimony on carbon nitride for the artificial photosynthesis of hydrogen peroxide. Nat. Catal. *4*, 374–384.

29. Chen, X., Shi, R., Chen, Q., Zhang, Z., Jiang, W., Zhu, Y., and Zhang, T. (2019). Three-dimensional porous g-C_3N_4 for highly efficient photocatalytic overall water splitting. Nano Energy *59*, 644–650.

30. Thaweesak, S., Wang, S., Lyu, M., Xiao, M., Peerakiatkhajohn, P., and Wang, L. (2017). Boron-doped graphitic carbon nitride nanosheets for enhanced visible light photocatalytic water splitting. Dalton Tran. *46*, 10714–10720.

31. Zhao, H., Liu, J., Li, C.F., Zhang, X., Li, Y., Hu, Z.-Y., Li, B., Chen, Z., Hu, J., and Su, B.-L. (2022). Meso-microporous nanosheet-constructed 3DOM perovskites for remarkable photocatalytic hydrogen production. Adv. Funct. Mater. *2112831*, 1–8.

32. Zhao, H., Li, C.F., Hu, Z.Y., Liu, J., Li, Y., Hu, J., Tendeloo, J., Chen, L.-H., and Su, B.-L. (2021). Size effect of bifunctional gold in hierarchical titanium oxide-gold-cadmium sulfide with slow photon effect for unprecedented visible-light hydrogen production. J. Colloid Interf. Sci. *604*, 131–140.

33. Zeng, Y., Liu, X., Liu, C., Wang, L., Xia, Y., Zhang, S., Luo, S., and Pei, Y. (2018). Scalable one-step production of porous oxygen-doped g-C_3N_4 nanorods with effective electron separation for excellent visible-light photocatalytic activity. Appl. Catal. B. *224*, 1–9.

34. Zhao, H., Liu, P., Wu, X., Wang, A., Zheng, D., Wang, S., Chen, Z., Larter, S., Li, Y., Su, B.-L., et al. (2021). Plasmon enhanced glucose photoreforming for arabinose and gas fuel co-production over 3DOM TiO_2-Au. Appl. Catal. B. *291*, 120055.

35. Wei, F.-Y., Liu, Y., Zhao, H., Ren, X., Liu, J., Hasan, T., Chen, L., Li, Y., and Su, B.-L. (2018). Oxygen self-doped g-C_3N_4 with tunable electronic band structure for unprecedentedly enhanced photocatalytic performance. Nanoscale *10*, 4515–4522.

36. Yücelen, E., Lazić, I., and Bosch, E.G. (2018). Phase contrast scanning transmission electron microscopy imaging of light and heavy atoms at the limit of contrast and resolution. Sci. Rep. *8*, 2676.

37. Zhang, W., Tian, Y., He, H., Xu, L., Li, W., and Zhao, D. (2020). Recent advances in the synthesis of hierarchically mesoporous TiO_2 materials for energy and environmental applications. Natl. Sci. Rev. *7*, 1702–1725.

38. Zhao, H., Hu, Z., Liu, J., Li, Y., Wu, M., Van Tendeloo, G., and Su, B.-L. (2018). Blue-edge slow photons promoting visible-light hydrogen production on gradient ternary 3DOM TiO_2-Au-CdS photonic crystals. Nano Energy *47*, 266–274.

39. Ding, Y., Maitra, S., Wang, C., Zheng, R., Zhang, M., Barakat, T., Roy, S., Liu, J., Li, Y., Hasan, T., et al. (2022). Hydrophilic bi-functional B-doped g-C_3N_4 hierarchical architecture for excellent photocatalytic H_2O_2 production and photo-electrochemical water splitting. J. Energy Chem. *70*, 236–247.

40. Li, Q., Anpo, M., and Wang, X. (2020). Application of photoluminescence spectroscopy to elucidate photocatalytic reactions at the molecular level. Res. Chem. Intermediat. *46*, 4325–4344.

41. Anpo, M., and Che, M. (1999). Applications of photoluminescence techniques to the characterization of solid surfaces in relation to adsorption, catalysis, and photocatalysis. Adv. Catal. *44*, 119–257.

42. Thanikaivelan, P., Padmanabhan, J., Subramanian, V., and Ramasami, T. (2002). Chemical reactivity and selectivity using Fukui functions: basis set and population scheme dependence in the framework of B3LYP theory. Theor. Chem. Acc. *107*, 326–335.

43. Parr, R.G. (1990). On the genesis of a theory. Int. J. Quan. Chem *37*, 327–347.

44. Zhang, B., Liao, S., Wu, W., Li, H., and Ren, T. (2018). Work function: a determining factor of the photodegradation rate of methyl orange via hollow octadecahedron Cu_2O crystals. Phys. Chem. Chem. Phys. *20*, 20117–20123.

45. Xia, P., Zhu, B., Cheng, B., Yu, J., and Xu, J. (2018). 2D/2D g-C_3N_4/MnO_2 nanocomposite as a direct Z-scheme photocatalyst for enhanced photocatalytic activity. ACS Sustain. Chem. Eng. *6*, 965–973.

46. Lohaus, C., Klein, A., and Jaegermann, W. (2018). Limitation of Fermi level shifts by polaron defect states in hematite photoelectrodes. Nat. Commun. *9*, 1–7.